Novel Co-Mn-O Nanosheet Catalyst for CO Preferential Oxidation Toward Hydrogen Purification

Zhongkui Zhao, Jinhan Lin, and Guiru Wang
State Key Laboratory of Fine Chemicals, Dept. of Catalysis Chemistry and Engineering, School of Chemical Engineering, Dalian University of Technology, Dalian 116024, P.R. China

Turghun Muhammad
Key Laboratory of Oil & Gas Fine Chemicals, Ministry of Education & Xinjiang Uyghur Autonomous Region, College of Chemistry & Chemical Engineering, Xinjiang University, Urumqi, Xinjiang 830046, China

DOI 10.1002/aic.14641
Published online October 10, 2014 in Wiley Online Library (wileyonlinelibrary.com)

Co-Mn-O composite oxide nanosheet catalyst was successfully prepared using a facile urea-assisted one-step hydrothermal method in the absence of organic or organic templating reagent. Co-Mn-O nanosheet catalyst was optimized by varying hydrothermal process parameters such as molar ratio of Co-Mn to urea, hydrothermal temperature, and hydrothermal time. Various characterization techniques including scanning electron microscopy, X-ray diffraction, nitrogen adsorption, X-ray photoelectron spectroscopy, Raman spectroscopy, and H_2 temperature-programmed reduction were used to reveal the relationship between catalyst nature and catalytic performance in CO preferential oxidation (CO PROX) in excess H_2. The developed Co-Mn-O nanosheet catalyst have demonstrated much superior catalytic performance to Co-Mn-O nanoparticle, particularly in the low temperature range, and 100% CO conversion over the developed Co-Mn-O nanosheet can be achieved in temperature range of 50 to 150°C at 10,000 mL g^{-1} h^{-1} of gas hourly space velocity in the standard feed. Furthermore, the almost complete CO removal over Co-Mn-O nanosheet at 125°C of low temperature with 94.9% selectivity can be achieved even in the simulated reformed gas. The excellent catalytic performance is ascribed to nanosheet morphology, more surface Co^{3+}, smaller average crystallite size, higher reducibility, and strong Co-Mn interaction. Catalytic stability investigation indicates the developed nanostructured catalyst exhibits high catalytic stability for CO PROX reaction in simulated gas. The developed Co-Mn-O nanosheet catalyst can be a potential candidate for catalytic elimination of trace CO from H_2-rich gas for Proton exchange membrane fuel cell applications. © 2014 American Institute of Chemical Engineers *AIChE J*, 61: 239–252, 2015
Keywords: CO preferential oxidation, Co-Mn-O nanosheet, morphology effect, H_2-rich gas, heterogeneous catalysis

Introduction

Proton exchange membrane fuel cell (PEMFC) is a promising highly efficient electronic apparatus with the clean H_2 as fuel.[1,2] H_2-rich stream is generally obtained from catalytic steam reforming of hydrocarbon or biomass and followed water gas shift (WGS) reaction.[3,4] However, owing to the limited activity of current WGS catalysts for complete CO conversion, a thermodynamically favored reaction at a low temperature, approximately 0.5–1.0 vol % of residual CO still remains in H_2-stream and requires to be lowered to less than 100 ppm to avoid poisoning the anode of PEMFC.[5,6] CO PROX reaction has been considered to be a straightforward and effective protocol for eliminating trace CO to purify hydrogen.[7–9] The CO PROX reaction unit can be attached to a PEMFC (typically working at 80–100°C) or to a WGS reactor (typically working at 200–250°C), or it can also be a medium unit between a Fuel Cell and a WGS reactor for immobile electricity-production station.[10] Therefore, to develop highly active and selective CO PROX, catalysts at low temperature with a wide temperature window is highly desirable.

Among a number of active catalysts reported for CO PROX, the precious metal-free copper-[11–13] and cobalt-[14–21] based catalysts have been generally accepted to be promising and interesting candidates in view of their high catalytic performance besides their good availability and low cost. Generally, copper-based catalysts exhibited high activity but narrow temperature window and also not satisfactory selectivity, and therefore, many efforts are continuously being made to improve their catalytic activity and selectivity and also to broaden temperature window for complete CO elimination from H_2-rich gas.[11–13,22–24] Hundred percent of CO conversion (40–60°C) of the highest activity toward copper-based catalyst has been reported recently,[22] which is most efficient catalyst for single CO PROX unit, but the narrow temperature window limits its flexibility of industrial applications.[10] Through fabricating inverse CeO_2/CuO configuration, the operation temperature window can be broadened to 60°C (90–150°C),[11,22–24] but the activity was obviously

Correspondence concerning this article should be addressed to Z. Zhao at zkzhao@dlut.edu.cn.

depressed after supporting Ce on Cu. As the other candidate for CO PROX, the cobalt-based catalysts have illustrated a wider temperature window for complete CO removal, but their catalytic activity at low temperature is definitely required to be improved.[14–21] In Dr. Zhongkui Zhao's "Nano Catalysis and Energy Storage" research group at Dalian University of Technology, recently, the continuing efforts are being made to improve catalytic performance especially catalytic activity at low temperature of cobalt-based catalysts,[25–35] and the Co-Mn-based catalysts have been considered to be a promising candidate, but the catalytic activity at low temperature is not satisfactory.[14–21,25–35] Therefore, further improvement in catalytic activity at low temperature is essential for practical applications in PEMFC. In this work, we would continuously put our full energy to improve the catalytic performance especially activity at low temperature of cobalt-based catalysts for CO PROX reaction.

The catalytic performance of heterogeneous catalysts is strongly dependent on their microstructure and surface chemistry, besides on their chemical elemental component.[36–39] Many reports have demonstrated that the nanostructured catalysts exhibit much superior catalytic properties to nanoparticulated ones for diverse reactions.[39–43] The previously reported nanosheet structured catalysts exhibited better catalytic performance to corresponding nanoparticles for catalytic oxidation and the photocatalysis in organic compound degradation and CO_2 reduction.[44–46] We envision that the Co-Mn-O nanosheet catalyst is expected to show superior catalytic performance in CO PROX reaction to its corresponding Co-Mn-O nanoparticle. However, to the best of our knowledge, no report on the CO PROX reaction catalyzed by the nanostructured Co-Mn-O catalysts can be found. In this work, Co-Mn-O composite oxide nanosheet was first successfully fabricated through a facile urea-assisted hydrothermal approach while no surfactants, templates, complex metal ligands, or fatty-acids was used to assist its growth. The as-prepared Co-Mn-O composite oxide nanosheet demonstrates much superior catalytic performance in CO PROX reaction with 100% CO conversion at 50°C of low temperature to the Co-Mn-O nanoparticle although they possess same elemental component. Furthermore, the catalytic performance of the Co-Mn-O nanosheet was optimized by varying the preparation parameters such as molar ratio of total Co and Mn atom to urea ($n_{\text{Co-Mn/Urea}}$), hydrothermal temperature (T_{hydroth}), and hydrothermal time (t_{hydroth}). Various characterization techniques including scanning electron microscopy (SEM), X-ray diffraction (XRD), nitrogen adsorption, X-ray photoelectron spectroscopy (XPS), Raman spectroscopy, and H_2 temperature-programmed reduction (H_2-TPR) were used to reveal the relationship between catalyst nature and catalytic performance in CO preferential oxidation in excess H_2. The high catalytic activity, wide temperature window for CO full removal, relatively good selectivity, and good catalytic stability, besides a facile and low-cost preparation method for the Co-Mn-O nanosheet allows it to be fascinating candidate for CO removal from H_2-rich gas.

Experimental Section

Catalyst preparation

The Co-Mn-O nanosheet catalyst was prepared by a urea-assisted hydrothermal method. In a typical synthesis, 2.328 g $Co(NO_3)_2{\cdot}6H_2O$ (Tianjin Bodi, AR), 0.245 g $Mn(CH_3COO)_2.4H_2O$ (Shenyang Reagent Corp., AR), and 10.8 g urea were first dissolved in 150 mL deionized water under vigorous stirring to form a homogeneous solution, and then, the mixture was continuously stirred for another 1 h. The solution was then transferred into a Teflon-lined autoclave. The autoclave was heated at 105°C for 6 h, and then naturally cooled down to room temperature. The resulted solid product was recovered by filtering and then washed by deionized water followed by ethanol. Finally, the obtained precursor was dried at 105°C overnight, and then calcined at 350°C in a muffle with a ramp rate of 1°C min^{-1} and kept for 5 h. The as-synthesized material with 8:1 of Co/Mn molar ratio was denoted as Co-Mn-O-ns. Then, Co-Mn-O nanoparticle was obtained using the same procedure as above except for urea being replaced by sodium carbonate, and the obtained Co-Mn-O nanoparticle was denoted as Co-Mn-O-np. Through varying the preparation parameters for Co-Mn-O-ns like $n_{\text{Co-Mn/Urea}}$ (4.5, 6, 9, 12, and 15), T_{hydroth} (90, 105, 120, 135, and 150°C), and t_{hydroth} (3, 6, 9, 12, and 18 h), a series of Co-Mn-O-ns catalysts were prepared. In all cases, the 8:1 of Co/Mn atomic ratio was used.

Catalysts characterization

SEM experiments were performed on JEOL JSM-5600LV SEM/EDX instrument. XRD patterns were collected from 10 to 80° at a step width of 0.02° using Rigaku Automatic X-ray Diffractometer (D/Max 2400) equipped with a CuKa source ($\lambda = 1.5406$ Å). The average crystalline particle size estimation was performed according to the Scherrer equation over multiple characteristic diffraction peaks. Nitrogen adsorption and desorption isotherms were determined on a Micromeritics apparatus of model ASAP-2050 system at −196°C. The specific surface areas were calculated by the Brunauer-Emmett-Teller method and the pore-size distributions were calculated from desorption branch of the isotherm by Barrett-Joyner-Halenda model. The Raman spectra were measured using a laser with an excitation wavelength of 633 nm at room temperature on a Thermo Scientific DXR Raman microscope. H_2-TPR experiments were performed in an in-house constructed system equipped with a thermal conductivity detector (TCD) to measure H_2 consumption. A quartz tube was loaded with 50 mg of catalyst which was pretreated by calcination in Ar at 300°C for 30 min and then was cooled to ambient temperature in Ar. After that, it was reduced with a 10 vol % H_2/Ar mixture (30 mL min^{-1}) by heating up to 800°C at a ramp rate of 10°C min^{-1}. XPS measurements were performed on a Thermo VG ESCALAB250 (Physical Electronics) using Al Kα radiation (1486.6 eV) as X-ray source. The binding energy was calibrated using C 1s photoelectron peak at 282.6 eV as a reference.

Catalytic performance measurement

The catalytic performance measurement experiments on the as-prepared catalysts were performed in a stainless steel, fixed-bed continuous-flow reactor (6 mm O.D.) at the atmospheric pressure. For each test, 100 mg catalyst with the defined particle size (200–250 mesh) was loaded between two quartz wool plugs. The temperature was measured by K-type thermocouples and controlled by a PID controller (Xiamen Yudian). Before the catalytic reaction test, the sample was pretreated at a rate of 10°C min^{-1} from the room temperature to 300°C in a 2.5 vol % O_2 flow (30 mL min^{-1}),

and kept for 30 min at 300°C. The reaction mixture was switched into fixed-bed reaction system after the sample being cooled to room temperature in an Ar flow. The feed contained 1.0 vol % O_2, 1.0 vol % CO, 50 vol % H_2, and the balance Ar, which is controlled by the mass flow controllers. The analysis of the feed and the effluent was performed using a gas chromatograph on-line equipped with a TCD and a flame ionized detector (FID). The mixture containing CO, O_2, H_2, and CO_2 were separated by combing the 5 A molecular sieve and PPQ columns. The trace CO and CO_2 were detected by FID after it being converted to methane by a methanation reactor (the CO and CO_2 gas chromatogram peaks can be clearly detected even if their concentration are less than 10 ppm), and O_2 detected by the TCD. The water vapor (10 vol %) and CO_2 (10 vol %) was introduced into the standard feed to obtain simulated reformed gas, and the catalytic performance of the developed catalyst for CO PROX reaction in simulated reformed gas was investigated. The effluent gas was first cooled by a condenser with ice water as coolant to remove H_2O before the gas flowing into chromatographic columns. No methane was detected over our catalysts in the temperature range from 30 to 220°C, which was consistent with the previous reports.[25–35]

CO conversion and O_2 selectivity to CO_2 were calculated on the basis of the CO and O_2 concentrations in the feed and the effluent ($[CO]_{in}$, $[CO]_{out}$, $[O_2]_{in}$ and $[O_2]_{out}$). The every point of the light-off curve is an average of three runs at isothermal conditions. CO conversion and O_2 selectivity to CO_2 were calculated on the basis of the equations as follows:

$$\text{CO conversion} \quad \chi_{CO}(\%) = \frac{[CO]_{in} - [CO]_{out}}{[CO]_{in}} \times 100$$

$$\text{O}_2\text{ conversion} \quad \chi_{O_2}(\%) = \frac{[O_2]_{in} - [O_2]_{out}}{[O_2]_{in}} \times 100$$

$$\text{H}_2\text{ conversion} \quad \chi_{H_2}(\%) = 2 \times \frac{\chi_{O_2} \times [O_2]_{in} - 0.5 \times \chi_{CO} \times [CO]_{in}}{[H_2]_{in}} \times 100$$

$$\text{O}_2\text{ selectivity to CO}_2 \quad S_{CO_2}(\%) = \frac{\chi_{CO}}{2 \times \chi_{O_2}} \times 100$$

Results and Discussion

Effect of Co-Mn-O morphology

The morphology of the as-prepared Co-Mn-O-ns and Co-Mn-O-np composite oxides were revealed by SEM, and the typical SEM images are presented in Figure 1. From Figure 1 (top), Co-Mn composite oxide nanosheet has been successfully fabricated by the facile and low-cost urea-assisted hydrothermal method. However, in replacement of urea by sodium carbonate, only the Co-Mn-O composite oxide particle can be obtained. The inset of Figure 1 (bottom) illustrates the Co-Mn-O-np is the aggregate containing nanoparticles with diverse sizes. The different morphologies of the as-prepared two samples by the same hydrothermal method but different precipitating agents may affect their catalytic performance for CO PROX reaction. The formation of sheet-structured materials may be resulted from the mediator role of urea decomposition.

Nitrogen adsorption experiments were used to investigate the surface areas and pore-size distributions of the as-prepared Co-Mn-O-ns and Co-Mn-O-np, and the nitrogen

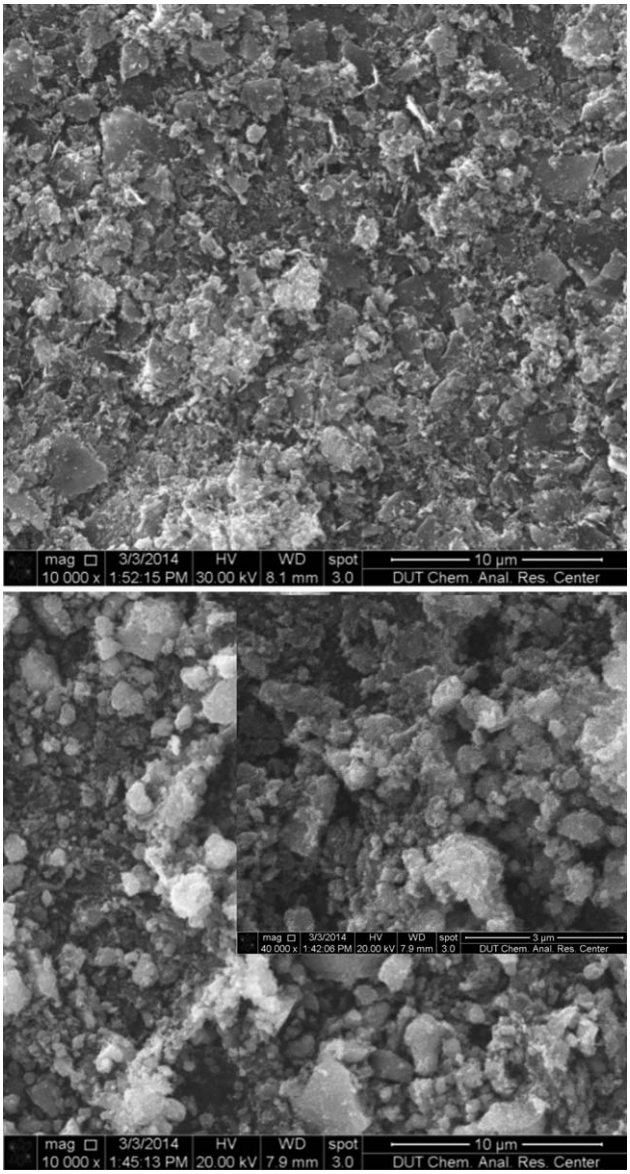

Figure 1. Typical SEM images of the as-synthesized Co-Mn-O-ns (top) and Co-Mn-O-np (bottom, inset in bottom: the magnified image).

adsorption-desorption isotherms of the two samples are presented in Figure 2, and the insets are Barrett-Joyner-Halenda pore-size distributions. The measurement results show the surface areas of as-prepared Co-Mn-O-ns and Co-Mn-O-np are 113.8 and 133.2 $m^2\ g^{-1}$, respectively, which are higher than that of pure Co_3O_4 prepared by the same method as that for Co-Mn-O-ns (48.4 $m^2\ g^{-1}$). Both of the isotherms are of type IV according to IUPAC classification and exhibits hysteresis loops with a featured capillary condensation in the mesopores. However, the isotherm corresponding to Co-Mn-O-ns shows the H3 hysteresis loop, indicating the presence of slit-shaped pores in this material possibly formed by the aggregation of sheet structures. The result further confirms the formation of nanosheet structure in Co-Mn-O-ns material, and the existed mesopores should be accumulating pores. From the pore-size distribution curves obtained from desorption branch, the Co-Mn-O-ns exhibits smaller pore size (4.0 nm) than that of Co-Mn-O-np (7.3 nm). The pore volume (determined at $p/p_0 = 0.996$) of Co-Mn-O-ns is also

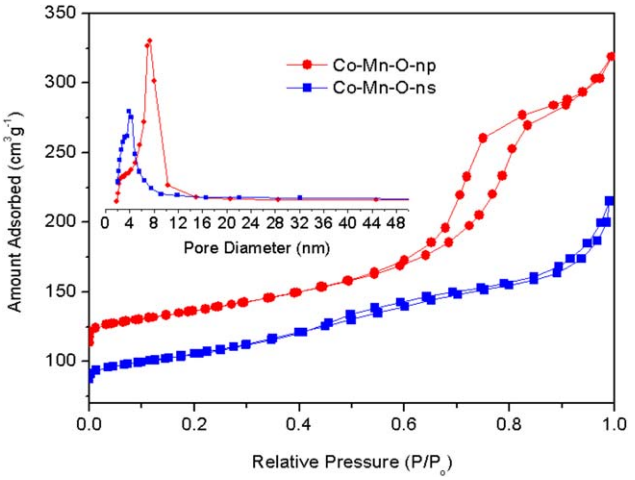

Figure 2. Nitrogen adsorption-desorption isotherms of the Co-Mn-O-ns and Co-Mn-O-np.

Insets: Barrett–Joyner–Halenda desorption pore-size distribution of the as-synthesized Co-Mn-O-ns and Co-Mn-O-np. [Color figure can be viewed in the online issue, which is available at wileyonlinelibrary.com.]

smaller (0.22 cm^3 g^{-1}) than that of Co-Mn-O-np (0.34 cm^3 g^{-1}). From above, the nanosheet-structured Co-Mn-O-ns prepared using urea as precipitating reagent possesses lower surface area, narrower pore size, and smaller pore volume than the Co-Mn-O-np prepared using sodium carbonate as precipitating agent.

Figure 3 demonstrates the catalytic performance of the as-prepared Co-Mn-O-ns and Co-Mn-O-np for the CO PROX reaction in excess H_2, and 15,000 mL h^{-1} g^{-1} of gas hourly space velocity (GHSV) is used. From Figure 3, the interesting thing is that, the Co-Mn-O-ns catalyst exhibits remarkably superior catalytic activity and comparison O_2 selectivity to CO_2 to Co-Mn-O-np, although the Co-Mn-O-np has higher specific surface area, larger pore volume, and bigger pore size than the Co-Mn-O-ns catalyst. Almost 100% CO conversion can be achieved over Co-Mn-O-ns catalyst in a wide temperature range of 60–200°C. Ninety-nine percent of CO conversion with 90% O_2 selectivity to CO_2 at the 60°C of low temperature can be obtained. However, only 33% CO conversion over Co-Mn-O-np catalyst can be obtained at 60°C. The catalytic activity of developed Co-Mn-O-ns catalyst has been close to that of precious metals reported in the references,[8,47] however, it illustrates very wide temperature operation window for the CO full removal. The as-prepared Co-Mn-O-ns catalyst via a facile and low-cost approach shows much higher catalytic activity than the previously reported Co-based catalysts. The catalytic performance of the developed Co-Mn-O-ns catalyst may be further improved by the following optimization process in this work. The catalytic activity of the as-prepared two Co-based samples for CO PROX reaction is notably dependent on their morphology, and Co-Mn-O composite oxide nanosheet exhibits much superior to Co-Mn-O-np.

Generally, the catalyst with higher specific area exhibits better catalytic performance especially better catalytic activity since the reaction takes place on the surface of heterogeneous catalyst. In this work, the Co-Mn-O-ns nanosheet catalyst has lower specific surface area but shows much higher catalytic activity than Co-Mn-O-np for CO PROX reaction. The further investigation on the nature of Co-Mn-O-ns catalyst to explore the structure-performance relationship and reveal the reason for its much better catalytic performance is highly desirable. Therefore, the XRD, XPS, Raman, and H_2-TPR characteristic techniques were used to further reveal the reasons why Co-Mn-O-ns nanosheet catalyst is much superior to Co-Mn-O-np nanoparticulate for CO PROX reaction, besides their different morphologies.

Figure 4 shows the XRD patterns of as-prepared Co-Mn-O-ns and Co-Mn-O-np prepared by hydrothermal method with urea and sodium carbonate as precipitating agent, respectively, as well as the pure Co_3O_4 prepared by the same process and preparation parameters as those for fabricating Co-Mn-O-ns is also included for comparison. From Figure 3, the XRD diffraction peaks of both Co-Mn-O-ns and Co-Mn-O-np samples at around 31.2, 36.9, 44.7, 55.9, 59.4, and 65.4° can be well resolved, which can be assigned to the (220), (311), (400), (422), (511), and (440) of crystalline planes of cubic spinel phase of Co_3O_4, respectively (JCPDS No. 74–1656).[48,49] In comparison of pure Co_3O_4 sample, the diffraction peaks of Co_3O_4 become broader and weaker for Co-Mn-O-ns and Co-Mn-O-np, suggesting the decrease in the crystalline sizes. Although no visible peak

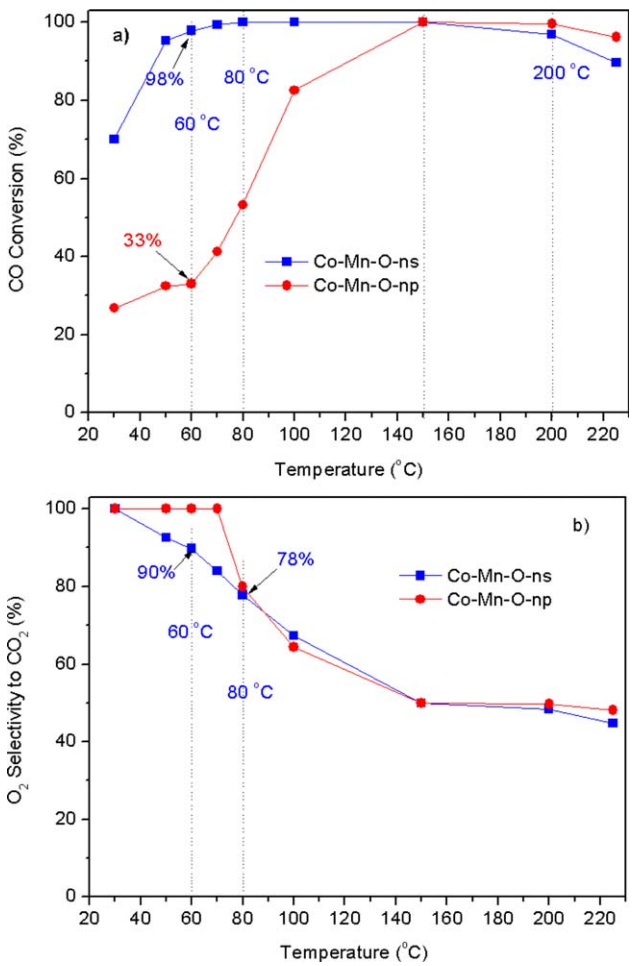

Figure 3. The CO conversion (a) and O_2 selectivity to CO_2 (b) over the as-synthesized Co-Mn-O-ns and Co-Mn-O-np.

Reaction conditions: 100 mg catalyst, GHSV = 15,000 mL h^{-1} g^{-1}, 1.0 vol % CO, 1.0 vol % O_2, 50 vol % H_2, Ar balance. [Color figure can be viewed in the online issue, which is available at wileyonlinelibrary.com.]

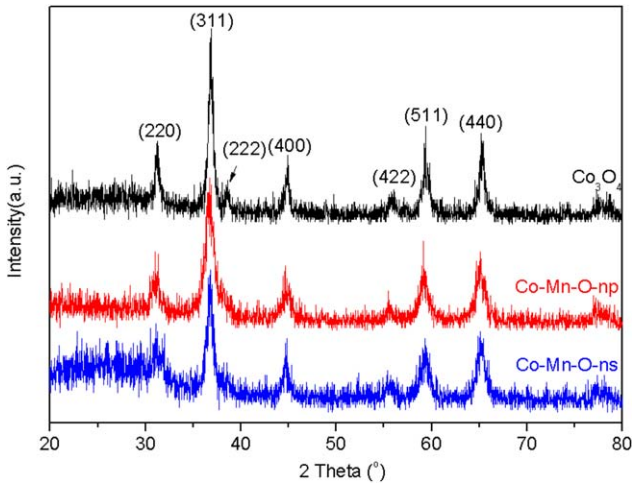

Figure 4. XRD patterns of the as-synthesized Co-Mn-O-ns and Co-Mn-O-np.

[Color figure can be viewed in the online issue, which is available at wileyonlinelibrary.com.]

corresponding to MnO_x can be resolved, the introduction of Mn into the Co-based composite oxides results in the decrease in crystalline size, which is consistent with the results those reported in the references.[15,48–50] We estimated the crystalline sizes of Co_3O_4 and the as-prepared two Co-Mn-O samples using the Scherrer equation. The calculated results demonstrate that the crystalline size for single-component Co_3O_4 sample is 20.3 nm, which is decreased to 15.1 and 15 nm for Co-Mn-O-ns and Co-Mn-O-np, respectively. Furthermore, in comparison of neat Co_3O_4, the shift of Co_3O_4 diffraction peaks to lower angles can be observed on the Co-Mn-O-ns and Co-Mn-O-np, suggesting the expansion in Co_3O_4 unit cell. The similar phenomena can be found in the previous reports,[15,25,29,35,48–50] which might be ascribed to the formation of $Mn_xCo_{3-x}O_4$ composite oxide phase owing to Mn insertion. The formation of $Mn_xCo_{3-x}O_4$ solid solution had been confirmed by X-ray absorption fine structure spectroscopy via analyzing the difference in coordination structures around Co and Mn atoms and the valence state of Mn species.[51,52] It can be identified that there can exist electron transfer between Co^{2+} and Mn^{4+} in the $Mn_xCo_{3-x}O_4$ composite oxide, and a partial Co^{2+} and Mn^{4+} may be transformed into Co^{3+} and Mn^{3+}/Mn^{2+}, respectively.[15,53] The lattice constants of Co_3O_4 unit cell for the MnO_x modified and unmodified catalysts are 5.7324 and 5.6992 Å, respectively. The enlargement occurs due to the replacement of Co^{3+} (0.64 Å) in the matrix by Mn^{3+} (0.66 Å), and Co^{2+} (0.78 Å) by Mn^{2+} (0.80 Å) with a slight larger ion radius. The change of Co^{2+} to Co^{3+} can result in the improved catalytic properties for CO PROX reaction.[15,33,51] However, from XRD analytical results, no obvious difference in the crystalline size and peak shift for Co-Mn-O-ns and Co-Mn-O-np can be observed, the further XPS and Raman characterization on the two samples are essential for revealing the relationship between the catalyst nature and catalytic performance in CO PROX reaction.

Both XPS and Raman spectroscopy are sensitive surface characterization techniques for surface chemistry. XPS and laser Raman techniques were used to identify surface chemical component and Co, Mn oxidation state in the Co-Mn-O-ns and Co-Mn-O-np samples. Figure 5 displays the XPS spectra in the Co $2p_{3/2}$, Mn $2p_{3/2}$ as well as O 1s regions for the two samples, and the details regarding curve-fitting data are summarized in Table 1. Shirley background was used to subtract curve background, and the 20% value of the fixed Lorentzian–Gaussian was used for peak fitting. The Co 2p3/2 peak region in the XPS spectra of both the samples can be deconvoluted into two spin-orbit doublets D1 and D2 as well as two satellite peaks (D1, D2, S1, S2) at 779.8/779.6, 781.6/78.7, 784.0/784.6, and 789.5/789.3 eV for the Co-Mn-O-ns and Co-Mn-O-np, respectively. The D1 peak and the two satellite peaks are associated to Co^{3+}, but the D2 peak can be assigned to Co^{2+}.[48,50] The much higher Co^{3+}/Co^{2+} on the Co-Mn-O-ns (4.08:1) than on the Co-Mn-O-np (1.03:1) can be observed. The Mn $2p_{3/2}$ region in the XPS spectra of the two samples can be fitted into two peaks at around 643.6 and 641.6 corresponding to Mn^{4+} and Mn^{3+}, respectively.[50,54] The developed Co-Mn-O-ns catalyst has a higher Mn^{4+}/Mn^{3+} ratio than that of Co-Mn-O-np. From above, although the same chemical component in the two samples, the different morphologies result in the diverse oxidation state for the surface Co and Mn species. The nanosheet-structured Co-Mn-O-ns composite oxide exhibits higher valent Co and Mn species on its surface than Co-Mn-O-np, which allows it to be much superior catalytic activity for CO PROX reaction. Moreover, the surface Co/Mn atomic ratio (11.35:1) from XPS analysis for the Co-Mn-O-ns is

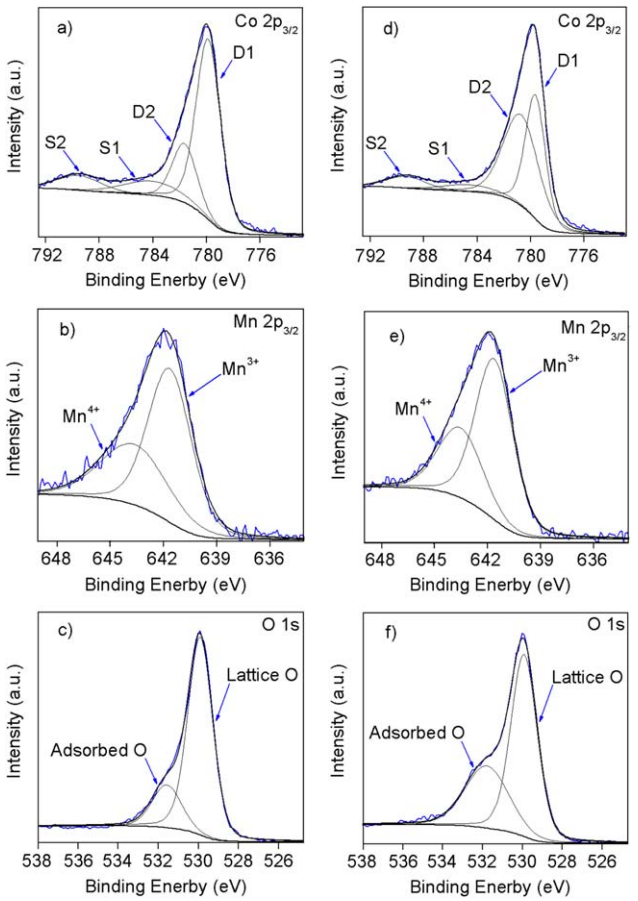

Figure 5. XPS spectra: Co $2p_{3/2}$ (a), Mn $2p_{3/2}$ (b), and O 1s (c) of Co-Mn-O-ns, as well as Co $2p_{3/2}$ (d), Mn $2p_{3/2}$ (e), and O 1s (f) of Co-Mn-O-np.

[Color figure can be viewed in the online issue, which is available at wileyonlinelibrary.com.]

Table 1. XPS Relative Intensity and Composition of the As-Synthesized Co-Mn-O-ns and Co-Mn-O-np

Relative Intensity		Co-Mn-O-ns B.E. (eV)/Composition (%)	Co-Mn-O-np B.E. (eV)/Composition (%)
Co $2p_{3/2}$ (%)	D1 peak	779.8/60.11	779.6/38.00
	D2 peak	781.6/19.67	780.7/49.16
	S1 peak	784.0/11.26	784.6/5.73
	S2 peak	789.5/8.96	789.3/7.11
Mn $2p_{3/2}$ (%)	Mn^{4+}	643.6/37.74	643.5/33.74
	Mn^{3+}	641.6/62.26	641.6/66.26
O 1s (%)	Adsorbed O	531.6/19.98	531.8/35.87
	Lattice O	529.9/80.02	529.9/64.13
Surface O Percentage[a]		67.76	73.11
	Adsorbed O	13.54	26.22
	Lattice O	54.22	46.89
Molar ratio[b]	Co^{3+}/Co^{2+}	4.08	1.03
	Mn^{4+}/Mn^{3+}	0.61	0.51
	Co/Mn[c]	11.35	4.67
	Co/Mn[d]	8	8

[a]The atom percentage of O atom to total atom amount of O, Co, and Mn from XPS analysis.
[b]Atom or cationic distribution.
[c]Surface Co/Mn atom ratio from XPS analysis.
[d]Bulk Co/Min atomic ratio, calculated on the basis of amount of the added Co and Mn in the process of preparing samples.

much higher than the bulk atomic ratio (8:1), however the lower surface atomic ratio of Co/Mn (4.67:1) of Co-Mn-O-np than bulk one (8:1) can be observed, suggesting Co enrichment on the surface of Co-Mn-O-ns, but Mn-enrichment on the surface of Co-Mn-O-np. That is to say, the morphology of Co-Mn composite oxide affects the surface Co/Mn ratio, and the nanosheet structured Co-Mn-O-ns sample is favorable for Co-enrichment on its surface. Both higher surface Co/Mn atomic ratio and higher Co^{3+}/Co^{2+} of the Co-Mn-O-ns demonstrates the more Co^{3+} absolute amount on its surface, which results in its higher catalytic activity than Co-Mn-O-np, now that Co^{3+} is the main active species for CO PROX reaction.[25–35] Moreover, as a first approximation Co enrichment could lead to higher electronegative sites (1.8) when compared to Mn (1.5), which may affect kinetics, and hence higher activity for Co-Mn-O-ns sheets. Furthermore, in the O 1s XPS peak region of both Co-Mn-O-ns and Co-Mn-O-np shown in Figures 5c, f, respectively, asymmetric two band structures can be observed. From references,[50,54] the fitted O 1s XPS peaks at around 529.9 and 531.6 eV of Co-Mn-O-ns (529.9 and 531.8 eV for Co-Mn-O-np) are assigned to the characteristic peaks corresponding to lattice O and adsorbed O, respectively. Correlated to reaction results, more surface lattice O is favorable for promoting the CO PROX catalytic activity of the Co-Mn-O-ns catalyst.

Laser Raman spectra on the Co-Mn-O-ns and Co-Mn-O-np, along with reference materials (neat Co_3O_4) are presented in Figure 6. From the feature of Raman spectra, the five strong peaks at 191, 470, 513, 609, and 673 cm^{-1} assigned to Raman-active modes depicted as $A_{1g} + E_g + 3F_{2g}$ of spinel structure of Co_3O_4 on the Raman spectra of the Co-Mn-O-ns and Co_3O_4 can be observed;[50,54] however, only very weak Raman peaks corresponding to Co_3O_4 spinel structure can be observed on the Raman spectrum of Co-Mn-O-np. This suggests more Co_3O_4 species, catalytically active for CO PROX reaction, on the Co-Mn-O-ns catalyst as compared to Co-Mn-O-np, which is consistent with the

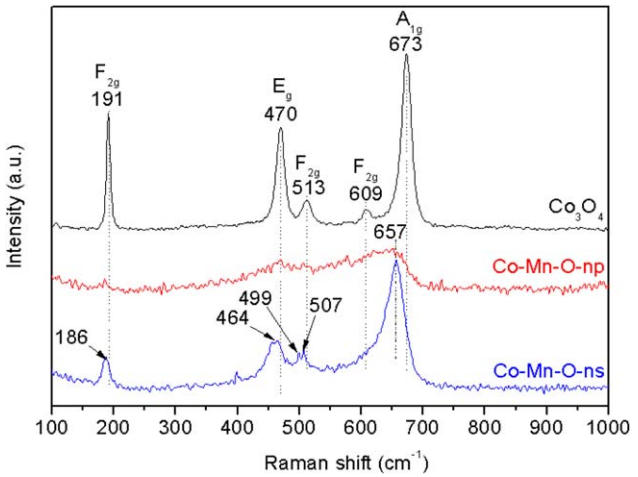

Figure 6. Raman spectra of the as-synthesized Co-Mn-O-ns and Co-Mn-O-np.

[Color figure can be viewed in the online issue, which is available at wileyonlinelibrary.com.]

results from XPS analysis shown as above. The broadened feature peaks corresponding to Co_3O_4 with a visible shift to lower wavenumber on Raman spectrum of Co-Mn-O-ns catalyst, in comparison of that of pure Co_3O_4, can be readily observed, suggesting the existence of strong interaction of Co-Mn.[29,33] This may lead to the increase in the catalytic performance of Co-based catalysts. The peak at 499 cm^{-1} on the Raman spectrum of Co-Mn-O-ns still keeps unknown, whether it plays an important role on promoting the catalytic performance needs to be further investigated. Moreover, no peaks corresponding to MnO_x can be observed on either Co-Mn-O-ns or Co-Mn-O-np, further suggesting the insertion of Mn into Co_3O_4 matrix, which is in good agreement with the results from XRD analysis.

Generally, the redox behavior of the oxide catalysts plays an important role in its catalytic performance for oxidation reactions. H_2-TPR profiles of the Co-Mn-O-ns and Co-Mn-O-np, along with reference material (pure Co_3O_4) are depicted in Figure 7. The profile of Co-Mn-O-ns or

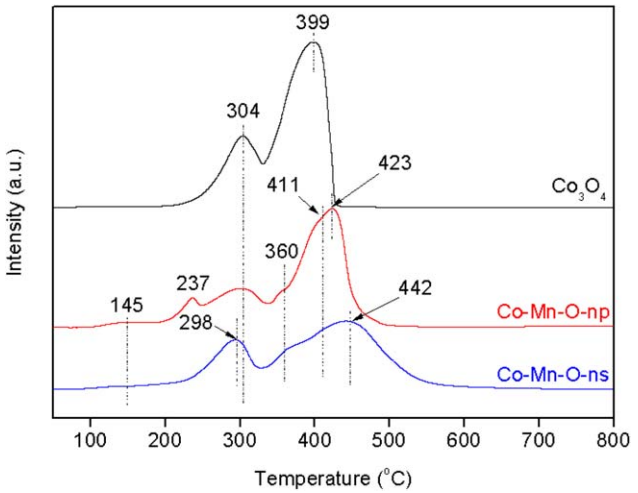

Figure 7. H_2-TPR profiles of the as-synthesized Co-Mn-O-ns and Co-Mn-O-np.

[Color figure can be viewed in the online issue, which is available at wileyonlinelibrary.com.]

Co-Mn-O-np can be divided into two zones. The peaks between 200 and 350°C can be assigned to the reduction of Co^{3+} to Co^{2+} and Mn^{4+} to Mn^{3+}, and the peaks after 350°C can be associated to the reduction of Mn^{3+} to Mn^{2+}, Co^{2+} to metal Co, or Mn^{2+} to metal Mn.[49,54] From our previous reports,[29,35] the first reduction peaks appearing before 350°C may decisively affect the catalytic performance, and therefore, the first reduction zone is further analyzed. The peak at around 145°C in the TPR profiles of the Co-Mn-O-ns and Co-Mn-O-np can be assign to the H_2 uptake for adsorbed O, indicating more adsorbed O on Co-Mn-O-np than on Co-Mn-O-s, which is in good agreement with the results obtained from XPS analysis. From XPS, more surface Mn species on the Co-Mn-O-np than on Co-Mn-O-ns, and therefore, the visible reduction peak appearing at 237 for Co-Mn-O-np may be surface Mn^{4+} (Owing to less surface M^{4+} and the shift of the peak at around 300°C to lower temperature on the Co-Mn-O-ns, the reduction peak of surface Mn^{4+} may merge into the reduction peak corresponding to Co^{3+} and bulk Mn^{4+}). The peak appears around at 300°C for Co-Mn-O-ns and Co-Mn-O-np can be assigned to the reduction of Co^{3+} to Co^{2+} and Mn^{4+} to Mn^{3+}. Owing to cobalt and manganese, oxides are reduced in the same temperature zone and presence of kinetic effects during the TPR measurement, which makes precise assignment of reduction peaks into individual chemical compounds extremely difficult. The reduction profiles may contain variable contributions from the samples. Therefore, the quantification of the peak area has not been taken into account. However, the peak corresponding to the reduction of Co^{3+} to Co^{2+} and Mn^{4+} to Mn^{3+} on the H_2-TPR profile of Co-Mn-O-ns shifts to lower temperature as compared to that of Co-Mn-O-np, which clearly indicates higher Co^{3+} and Mn^{4+} reducibility in Co-Mn-O-ns than that in Co-Mn-O-np. Correlated to the reaction results, the higher reducibility of Co^{3+} and Mn^{4+} is favorable for catalytic activity in CO PROX reaction.

Optimization of Co-Mn-O-ns catalyst

Through optimizing the hydrothermal process conditions, we wish to further improve the catalytic performance of the developed Co-Mn-O-ns nanostructure catalyst. Herein, we investigated the effect of $n_{Co\text{-}Mn/Urea}$, $T_{hydroth}$, and $t_{hydroth}$ on the catalyst nature and catalytic performance in CO PROX reaction in excess H_2. Effect of $n_{Co\text{-}Mn/Urea}$ was investigated by varying the amount of added Co and Mn precursors but fixing the amount of added urea and water. Figure 8 presents the catalytic reaction results. From Figure 8a, as the increase of $n_{Co\text{-}Mn/Urea}$, the catalytic activity arises and reaches maximum while the $n_{Co\text{-}Mn/Urea}$ is increased up to 9, then the catalytic activity decreases as the $n_{Co\text{-}Mn/Urea}$ is further increased. The Co-Mn-O-ns catalyst with the 9 of $n_{Co\text{-}Mn/Urea}$ exhibits the best catalytic activity, and 95.3%, 97.9%, and 99.4% of CO conversion can be obtained at the reaction temperatures of 50, 60, and 70°C, respectively. However, only 82.5%, 88.7%, and 95.2% of CO conversion can be obtained at their corresponding reaction temperatures over the Co-Mn-O-ns catalyst with the 15 of $n_{Co\text{-}Mn/Urea}$. From Figure 8b, Co-Mn-O-ns catalyst with the nine of $n_{Co\text{-}Mn/Urea}$ also exhibits superior O_2 selectivity to CO_2 than Co-Mn-O-ns catalyst with the 15 of $n_{Co\text{-}Mn/Urea}$. Then XRD, Raman, and H_2-TPR experiments on the three Co-Mn-O-ns samples with 4.5, 9, and 15 of $n_{Co\text{-}Mn/Urea}$ were performed to reveal the reason why the nine of $n_{Co\text{-}Mn/Urea}$ is optimal but both

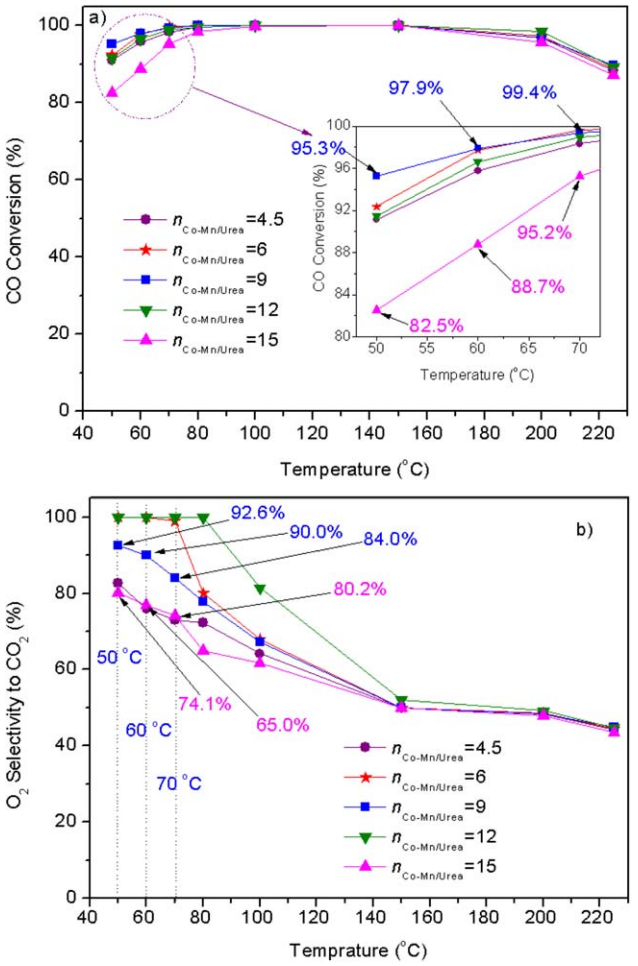

Figure 8. The CO conversion (a) and O_2 selectivity to CO_2 (b) over the Co-Mn-O-ns samples prepared with diverse $n_{Co\text{-}Mn/Urea}$.

Reaction conditions: GHSV = 15,000 mL h^{-1} g^{-1}, 1.0 vol % CO, 1.0 vol % O_2, 50 vol % H_2, Ar balance. [Color figure can be viewed in the online issue, which is available at wileyonlinelibrary.com.]

too high and too low $n_{Co\text{-}Mn/Urea}$ depresses catalytic performance of the as-prepared Co-Mn-O-ns catalysts. XRD and H_2-TPR characterization results are presented in Figure 9.

From Figure 9a, $n_{Co\text{-}Mn/Urea}$ does not lead to visible change in XRD patterns, but affects the intensity and peak width. The weaker and broader characteristic peaks on Co-Mn-O-n with nine of $n_{Co\text{-}Mn/Urea}$ than those of others can be observed, implying the smaller average crystalline size of Co_3O_4 nanocrystal. The average crystalline sizes of Co_3O_4 for the three samples were estimated by the Scherrer equation. The size for three samples with 4.5, 9, and 15 of $n_{Co\text{-}Mn/Urea}$ are 16.1, 15.0, and 17.2 nm, respectively. As is known, the added Co-Mn concentration can simultaneously affect both crystalline core formation and its growth. The less crystalline core amount led by low Co-Mn concentration can result in larger crystalline particle. The increase in Co-Mn concentration may result in quick formation of more crystalline core, on the other side of the coin, too high concentration may also lead to further grown of the core into larger crystalline particle. The average crystalline size of the samples may remarkably affects Co-Mn interaction, reducibility, and the selective adsorption behavior of CO and H_2

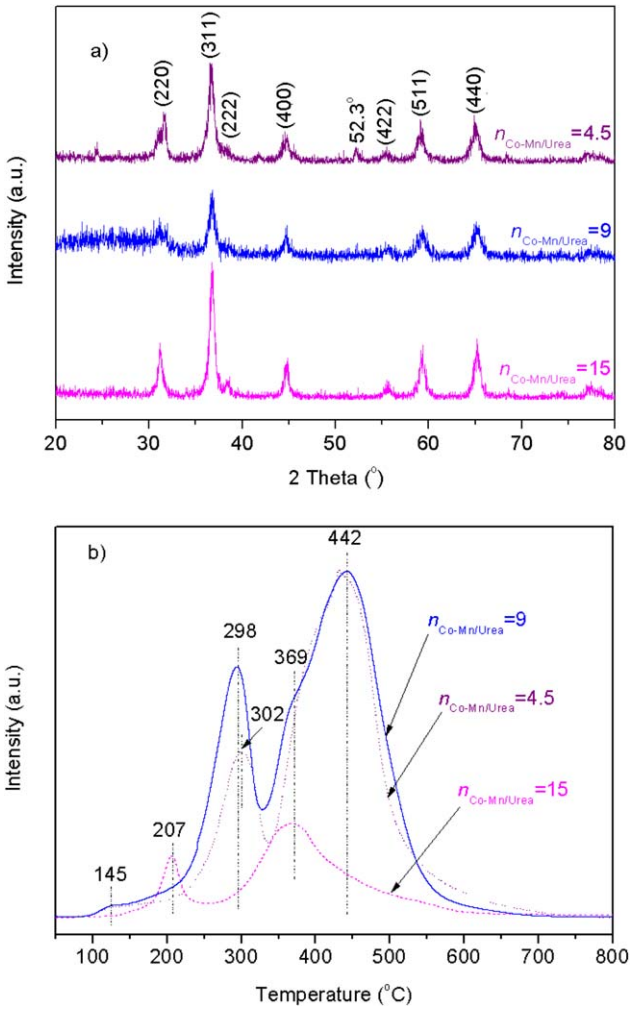

Figure 9. XRD patterns (a) and H_2-TPR profiles (b) of the Co-Mn-O-ns samples prepared with diverse $n_{Co\text{-}Mn/Urea}$.

[Color figure can be viewed in the online issue, which is available at wileyonlinelibrary.com.]

molecules, and therefore can further affect the catalytic performance in CO PROX reaction. The smallest average crystalline size may be one reason for its highest catalytic performance, especially catalytic activity. From Figure 9b, the H_2-TPR profiles can be divided into two peaks. In comparison of the reducible behavior of Co-Mn-O-ns ($n_{Co\text{-}Mn/Urea} = 4.5$), the lower reduction temperature and higher H_2 uptake for the first reduction peak corresponding to the reduction of Co^{3+} to Co^{2+} and the Mn^{4+} to Mn^{3+} while the similar reduction temperature and H_2 consumption of the second peak corresponding to reduction of Mn^{3+} to Mn^{2+}, Co^{2+} to metal Co, or Mn^{2+} to metal Mn of the Co-Mn-O-ns with nine of the $n_{Co\text{-}Mn/Urea}$ can be found, suggesting the higher reducibility of Co-Mn-O-ns ($n_{Co\text{-}Mn/Urea} = 9$). As a result, Co-Mn-O-ns ($n_{Co\text{-}Mn/Urea} = 9$) exhibits better catalytic performance in CO PROX reaction. H_2-TPR profile of Co-Mn-O-ns ($n_{Co\text{-}Mn/Urea} = 15$) shows the least H_2-uptake for both the first and the second reduction peaks. The much less reducible Co-Mn-O leads to the decrease in both CO and H_2 oxidation, especially leads to the more decrease in CO conversion. Therefore, Co-Mn-O-ns ($n_{Co\text{-}Mn/Urea} = 15$) shows both lower activity and lower selectivity for CO PROX reaction in excess H_2.

Hydrothermal temperature may affect the hydroxyl ion concentration via the controllable hydrolysis of urea. At the same time, the hydrothermal temperature and its resulting changeable hydroxyl ion concentration can significantly affect the kinetics of formation and growth of Co-Mn-O crystalline core, and therefore affects the catalytic performance of the resulted Co-Mn-O-ns catalysts. Herein, the effect of hydrothermal temperature on catalytic performance and catalyst nature was investigated by varying hydrothermal temperatures from 90 to 150°C. Reaction and characterization results are depicted in Figures 10 and 11, respectively.

From Figure 10a, with the increase in hydrothermal temperature, the catalytic activity increases, and reaches maximum CO conversion over the Co-Mn-O-ns ($T_{hydroth} = 135$°C) following decreases as the hydrothermal temperature is increased up to 150°C. From Figure 10b, the effect of hydrothermal temperature on the selectivity is not well regular. Co-Mn-O-ns catalyst prepared using 135°C of $T_{hydroth}$ exhibits much superior catalytic activity and good selectivity, and almost complete CO removal can be obtained at the wide temperature window of 60–200°C. From Figure 11a, the cubic Co_3O_4 crystal plane with $Fd\bar{3}m$ crystallite type is identified in comparison of the corresponding JCPDS file (74–1656). For all samples prepared with different hydrothermal temperatures, no MnO_x phase maybe resolved, suggesting no phase separation of the samples although different hydrothermal temperatures are used, is in good agreement with the previous reported results.[15,48–50] Similar to the XRD results corresponding to effect of $n_{Co\text{-}Mn/Urea}$ shown as above, the change in hydrothermal temperature mainly results in difference in XRD peak intensity and width. The average crystalline size of Co_3O_4 in the Co-Mn-O-ns samples estimated from XRD characteristic peaks are 15.7, 14.5, and 15.3 nm corresponding to the hydrothermal temperature of 90, 135, and 150°C, respectively. As is shown in the above analysis, the smaller average crystalline for Co_3O_4 in the Co-Mn-O-ns samples is favorable for better catalytic performance in CO PROX reaction. From 11b, in comparison of the H_2-TPR profile of Co-Mn-O-ns ($T_{hydroth} = 90$°C), the reduction temperature corresponding to the latter peak of the H_2-TPR profile of Co-Mn-O-ns ($T_{hydroth} = 135$°C) is much lower, although similar reduction temperature and less H_2 consumption corresponding to the first reduction peak can be observed. Correlated to catalytic reaction results, the reduction behavior of Mn^{3+} to Mn^{2+}, Co^{2+} to metal Co, or Mn^{2+} to metal Mn affects the catalytic performance of Co-Mn-O-ns, although the Co_3O_4 is main active species. That is to say, the catalytic performance of Co-Mn-O-ns rests on the first reduction peak of the H_2-TPR profile corresponding to the reduction of Co^{3+} and Mn^{4+}, and it is also affected by the latter reduction peak feature. However, the reason why the reduction temperature corresponding to second peak on the H_2-TPR profile of Co-Mn-O-ns ($T_{hydroth} = 90$°C) shifts to a higher temperature remains to be resolved. It would be full addressed in the future research. Furthermore, in comparison of Co-Mn-O-ns ($T_{hydroth} = 150$°C), the H_2 uptake for the first reduction peak of the Co-Mn-O-ns ($T_{hydroth} = 135$°C) is larger, and the reduction temperature is lower, ascribed to better Co-Mn interaction while it is prepared at lower temperature. By comparing the three samples, we can see that lower reduction temperature and larger H_2 uptake corresponding to first

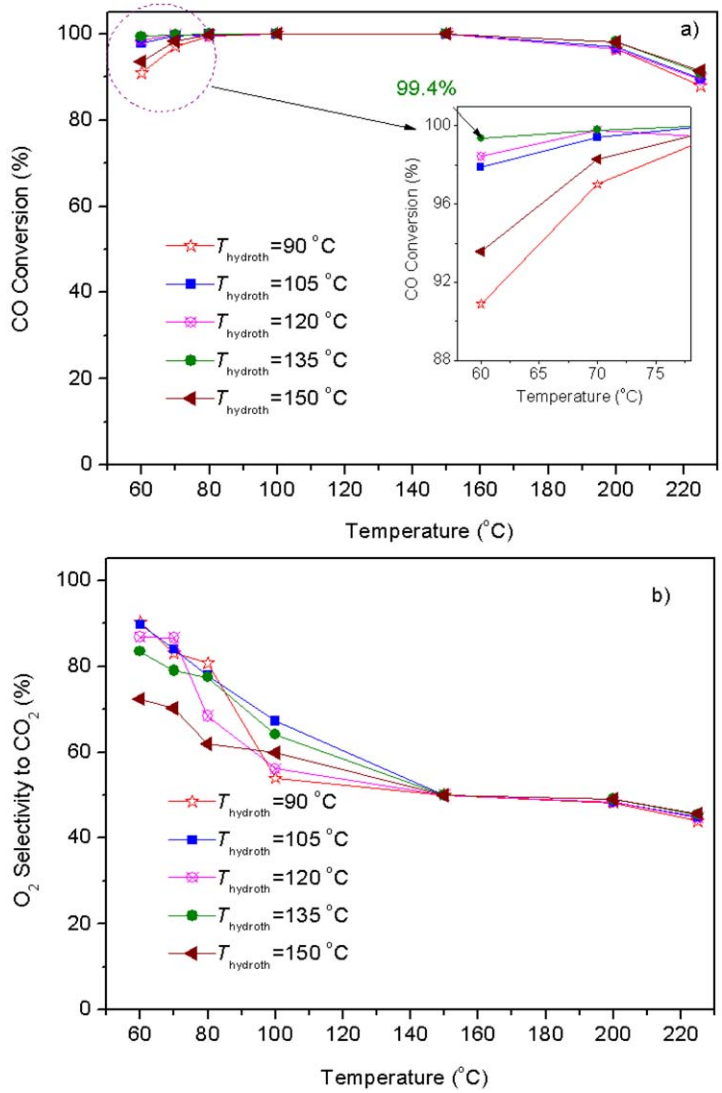

Figure 10. The CO conversion (a) and O_2 selectivity to CO_2 (b) over the Co-Mn-O-ns samples prepared with diverse $T_{hydroth}$.

Reaction conditions: GHSV = 15,000 mL h^{-1} g^{-1}, 1.0 vol % CO, 1.0 vol % O_2, 50 vol % H_2, Ar balance. [Color figure can be viewed in the online issue, which is available at wileyonlinelibrary.com.]

reduction peak appear on the samples that prepared with lower hydrothermal temperature, which may be ascribed to the stronger Co-Mn interaction while the Co-Mn interaction may be weakened by the quicker precipitation and crystallization at higher hydrothermal temperature. On the basis of above analysis, the 135°C of optimum hydrothermal temperature is required for excellent catalytic performance.

Furthermore, the effect of hydrothermal time on the catalyst nature and catalytic performance were investigated by preparing a series of Co-Mn-O-ns catalysts with diverse hydrothermal times varying from 3 to 18 h. Figure 12 presents the reaction results. The results show that the catalytic activity arises and then reaches the maximum value as the hydrothermal temperature is prolonged from 3 to 9 h, and the further prolonging hydrothermal time leads to a visible decrease in CO conversion. Nine hours of optimal hydrothermal time is essential to obtain satisfactory catalytic performance. Hundred percent of CO conversion with 8% of selectivity (Figure 11b) at 60°C of lower reaction temperature over the Co-Mn-O-ns ($t_{hydroth}$) catalyst can be achieved, and even the CO conversion reaches about 97% at the 50°C of lower reaction temperature. Our previously reported hierarchically nanoporous Co-Mn/FeO_x has exhibited unexpected catalytic performance, and the 100% CO conversion at 75°C can be achieved.[25] However, the hexadecyltrimethylammonium bromide as organic template agent and the monodispersed SiO_2 microsphere as inorganic template are required in the synthetic process, besides the multistep process for its preparation, which limits its practical application. In this work, the Co-Mn-O-ns catalyst with superior catalytic performance to the reported hierarchically nanoporous Co-Mn/FeO_x for CO PROX reaction can be prepared by a facile one-step urea-assisted hydrothermal approach, in which only low-cost urea but no any other template agent is used. Therefore, the developed Co-Mn-O-ns catalyst with optimized preparation conditions could be considered as a potential and practical catalyst for H_2 purification through CO PROX reaction.

To reveal the structure-performance relationship of the Co-Mn-O-ns catalysts with diverse hydrothermal times, the XRD and H_2-TPR experiments were performed, and the XRD patterns and H_2-TPR profiles are presented in Figure

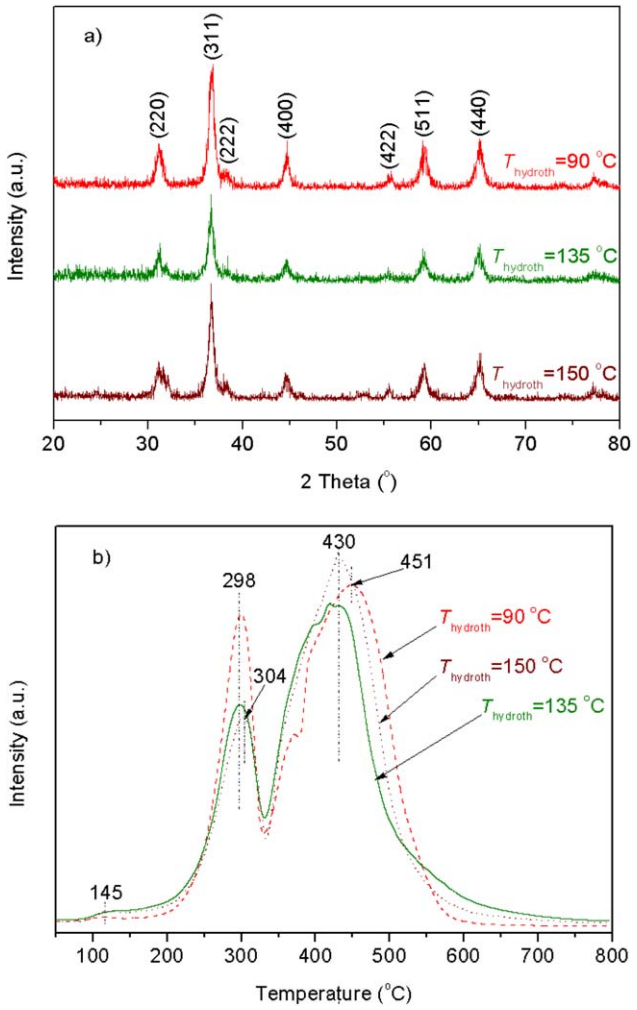

Figure 11. XRD patterns (a) and H_2-TPR profiles (b) of the Co-Mn-O-ns samples prepared with diverse $T_{hydroth}$.

[Color figure can be viewed in the online issue, which is available at wileyonlinelibrary.com.]

13. From Figure 13a, the weaker and broader XRD characteristic peaks corresponding to Co_3O_4 phase on the XRD pattern of Co-Mn-O-ns catalyst prepared with the 9 h of hydrothermal time than those of other two can be observed, suggesting no CoO_x and MnO_x phase separation as well as smaller average crystalline size, which may be favorable for its higher catalytic performance. Although longer hydrothermal time may be favorable for obtaining relatively homogeneous particle through a dissolving of larger particle and further growing procedure of smaller particle, the Co-Mn-O-ns catalyst prepared with the 18 h of hydrothermal time exhibits worse catalytic performance in CO PROX reaction. From Figure 13b, it can be found that the prolonging hydrothermal time can lead to the first reduction peak corresponding to the reduction of Co^{3+} and Mn^{4+} shift to lower temperature; however, it also results in the decrease in H_2 uptake. The former is favorable for CO PROX reaction, but the latter is unfavorable. Furthermore, the similar reduction temperature and H_2-uptake for the second reduction peak can be seen. Therefore, the optimum hydrothermal time is required for achieving best catalytic performance.

Effect of GHSV in standard feed

GHSV is one of the significant technical parameters for industrial process. Therefore, we investigate the effect of GHSV on the catalytic performance of optimized Co-Mn-O-ns catalyst for CO PROX reaction, and the reaction results are demonstrated in Figure 14. Results show that the developed Co-Mn-O-ns catalyst exhibits excellent catalytic performance with 100% CO conversion with 72% of selectivity at 50°C and a wide temperature window of 50–150°C (more than 97% CO conversion at 200°C) for CO complete removal via CO PROX reaction in excess H_2. Even if the reaction is run at 30,000 mL h^{-1} g^{-1}cat of high GHSV, 100% of CO conversion at 100°C can also be achieved, implying the high catalytic efficiency.

Effect of H_2O and CO_2 in the feed

Generally, the H_2-rich reformed gas obtained from reforming process for PEMFCs also contains certain amount of CO_2 and H_2O, so the research on the catalytic performance of the catalyst on CO PROX reaction under the simulated reformed gas is essential for possibly practical application. CO PROX reaction test was performed over the optimized

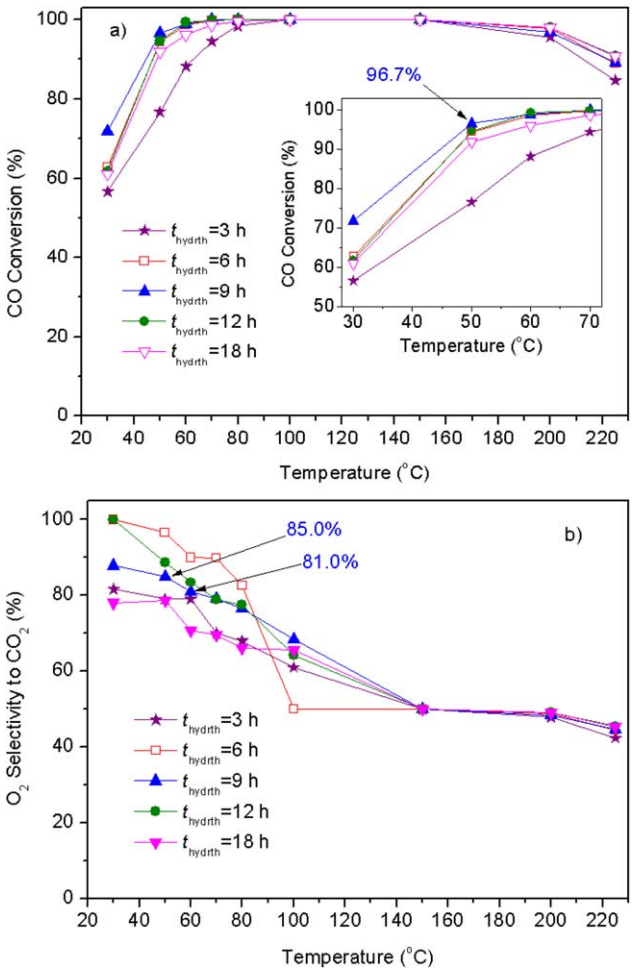

Figure 12. The CO conversion (a) and O_2 selectivity to CO_2 (b) over the Co-Mn-O-ns samples prepared with diverse $t_{hydroth}$.

Reaction conditions: GHSV = 15,000 mL h^{-1} g^{-1}, 1.0 vol % CO, 1.0 vol % O_2, 50 vol % H_2, Ar balance. [Color figure can be viewed in the online issue, which is available at wileyonlinelibrary.com.]

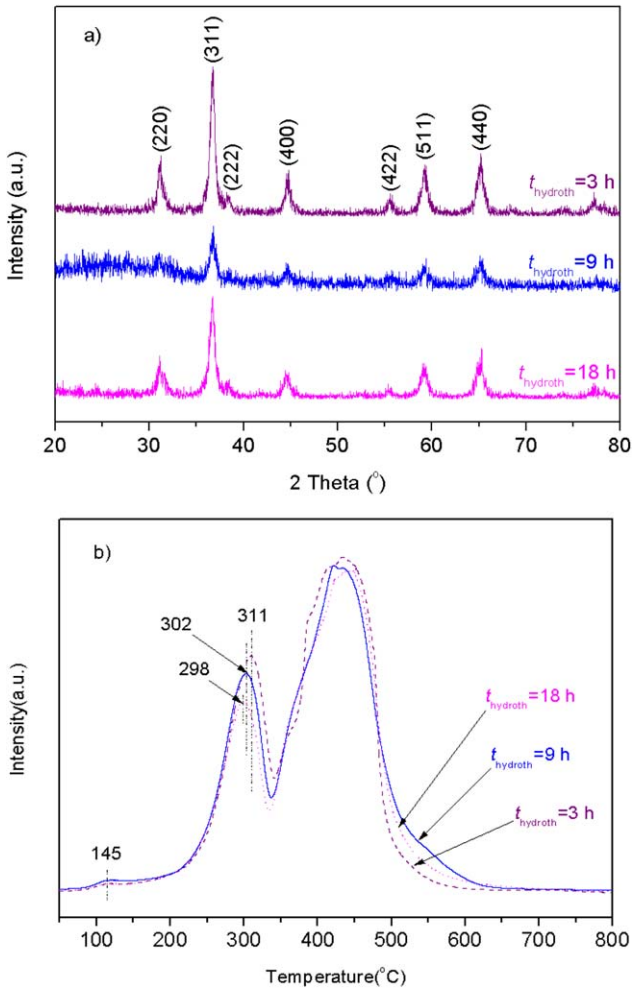

Figure 13. XRD patterns (a), H_2-TPR profiles (b), and Raman spectra (c) of the Co-Mn-O-ns samples prepared with diverse $t_{hydroth}$.

[Color figure can be viewed in the online issue, which is available at wileyonlinelibrary.com.]

Co-Mn-O-ns catalyst using simulated reformed gas as feed (10 vol % H_2O and 10 vol % CO_2 being introduced) and in standard feed. Reaction results are presented in Figure 15, and the catalytic performance of Co-Mn-O-np in presence (simulated real feed) and absence (ideal feed) of CO_2 and H_2O also included for comparison. From Figure 15, it can be observed that, the 100% CO conversion in a temperature range of 150–200°C can be obtained over the developed Co-Mn-O-ns catalyst in the simulated reformed gas, although CO conversion decreases in comparison of that under standard feed gas. However, in comparison of Co-Mn-O-ns, the Co-Mn-O-np shows much inferior catalytic performance in either ideal feed or simulated real feed, and no complete conversion can be observed in the simulated reforming gas. It is demonstrated that the developed Co-Mn-O-ns catalyst is superior to Co-Mn-O-np for CO PROX reaction in either ideal feed or simulated real feed. Moreover, for both of them (np and ns), the decreased catalytic activity can be obtained in simulated real feed. The negative effect brought by H_2O is mainly attributed to the blockage of active sites on the surface of catalyst owing to competitive adsorption, suppressing the activation of CO and O_2.[15] While the inhibiting effect brought by CO_2 was reported to be the forming of carbonates by adsorption of CO_2 on active sites,[21,55] as well as the competitive adsorption of CO and CO_2 on catalyst surface.[56] By varying GHSV and O_2 concentration (Figure 15), complete CO removal with 89.3% of selectivity can be achieved at 135°C, as well as the almost 100% of CO conversion with 94.9% of selectivity. The almost 100% of CO conversion in a very wide temperature 125–225°C in the simulated reformed gas can be achieved, which is much wider than the reported 5–20°C operation window width in references.[57–59] The developed Co-Mn-O-ns catalyst shows better catalytic performance than all of our previously reported Co-based catalysts under simulated reformed gas for CO PROX reaction.[25–35]

Stability investigation

The deactivation during CO PROX reaction process is a serious problem for Co-based catalysts.[27,41,60] In this study, we investigated the stability of the developed novel Co-Mn-O-ns catalyst in simulated reformed gas. Reaction results are listed in Figure 16. The results show that no obvious change

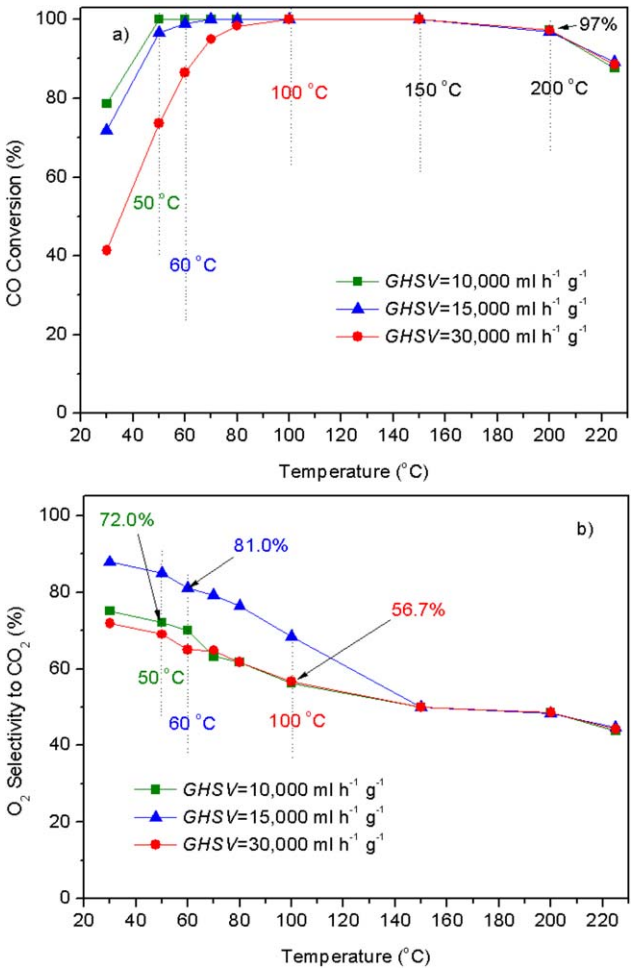

Figure 14. Effect of GHSV on the CO conversion (a) and O_2 selectivity to CO_2 (b) for the CO PROX reaction in excess H_2 over the optimized Co-Mn-O-ns catalyst in standard gas feed.

Reaction conditions: 1.0 vol % CO, 1.0 vol % O_2, 50 vol % H_2, Ar balance. [Color figure can be viewed in the online issue, which is available at wileyonlinelibrary.com.]

can be observed in CO conversion but an increase in O_2 selectivity to CO_2 during the reaction process in simulated reformed gas. The good stability of Co-Mn-O-ns catalyst may be resulted from the previously established increase in amount of active oxygen species and adsorbed CO, as well as the enhancement in stability of Co_3O_4 by adding suitable amount of MnO_x into the composite.[15,33]

From above, almost complete CO removal could be achieved over the developed catalyst in this article in a wide temperature window of 50–150°C. Although the catalytic activity decreased with the addition of H_2O and CO_2 in feed, the almost 100% CO conversion could be still maintained at 125–225°C (100°C), which was a much wider operation temperature window compared with the reported 5–20°C.[57–59] Co-Mn-O-ns catalyst exhibits excellent catalytic performance in excess H_2 and even in simulated reformed gas, as well as

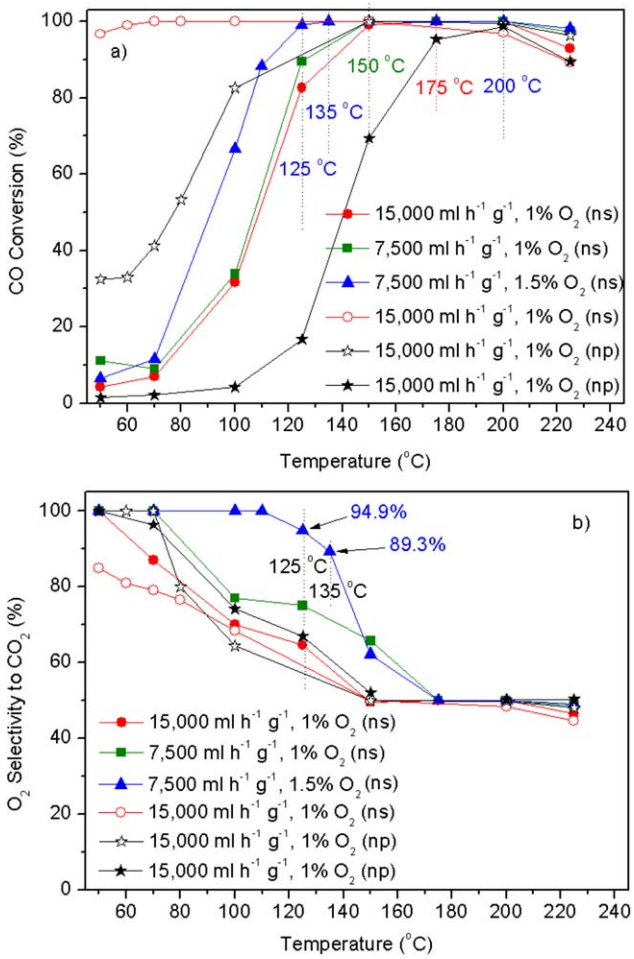

Figure 15. Effect of VHSV and O_2 concentration on the CO conversion (a) and O_2 selectivity to CO_2 (b) for the CO PROX reaction over the optimized Co-Mn-O-ns catalyst in simulated reformed gas (solid symbol) and in standard gas (open symbol), the results for the Co-Mn-O-np in the presence and absence CO_2 and H_2O at 15,000 mL h^{-1} g^{-1} GHSV are included for comparison.

Reaction conditions: 1.0 vol % CO, 50 vol % H_2, Ar balance. Ten volume percent of H_2O and 10 vol % CO_2 were introduced for simulated reformed gas. [Color figure can be viewed in the online issue, which is available at wileyonlinelibrary.com.]

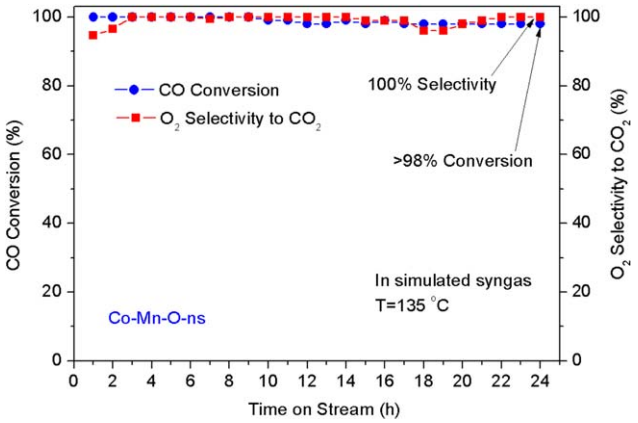

Figure 16. CO conversion and O_2 selectivity to CO_2 as a function of time on stream for the CO PROX reaction over the developed Co-Mn-O-ns catalyst in simulated reformed gas.

Reaction conditions: GHSV = 7500 mL h^{-1} g^{-1}, 1.0 vol % CO, 1.5 vol % O_2, 10 vol % H_2O and 10 vol % CO_2, 50 vol % H_2, Ar balance. [Color figure can be viewed in the online issue, which is available at wileyonlinelibrary.com.]

the composite catalyst can overcome the easy leaching problem of active component from the supported catalyst, besides, CO conversion over the as-prepared Co-Mn-O-ns catalyst has no obvious change during the reaction process at 135°C in simulated reformed gas with almost 100% selectivity, implying its outstanding CO_2 and H_2O resistance. Furthermore, the developed catalyst was obtained by a facile and low-cost one-pot urea-assisted hydrothermal method, which allows it to be a practical catalyst for CO removal from hydrogen-rich stream.

Conclusions

In this work, we have successfully prepared Co-Mn-O-ns nanosheet catalyst through a facile and low-cost one-pot urea-assisted hydrothermal approach. The developed Co-Mn-O-ns catalyst exhibits much superior catalytic performance in CO PROX reaction. The as-prepared Co-Mn-O-ns catalyst has been optimized. The optimized catalyst exhibits excellent catalytic performance with almost complete CO removal in a wide temperature window of 50–150°C, and even in simulated reformed gas, almost 100% CO conversion could still be achieved at 125°C, and in a very wide temperature of 125–225°C (100°C), which was a much wider operation temperature window compared with the reported 5–20°C. The excellent catalytic performance of the developed Co-Mn-O-ns catalyst is remarkably dependent on the nanosheet morphology, more amount of surface Co^{3+}, smaller average crystalline size, strong Co-Mn interaction, and the reducibility, affected by the precipitating reagent type and hydrothermal conditions in the preparation procedure. CO conversion over the as-prepared Co-Mn-O-ns catalyst has no obvious change during the reaction process at 135°C in simulated reformed gas with almost 100% selectivity, implying its outstanding catalytic stability. The composite oxide-type catalyst can overcome the easy leaching problem of active component from the supported-type catalyst. Furthermore, the facile and low-cost one-pot urea-assisted hydrothermal approach is used to prepare Co-Mn-O-ns catalyst. In

combination of excellent catalytic activity, selectivity, stability, and the easy and low-cost preparation, the developed Co-Mn-O-ns catalyst can be considered as a practical candidate for CO removal from hydrogen-rich stream.

Acknowledgments

This work is financially supported by the National Natural Science Foundation of China (20803006, 21276041, U1261104), also sponsored by Key Laboratory of Oil & Gas Fine Chemicals, Ministry of Education & Xinjiang Uyghur Autonomous Region, Xinjiang University (XJDX0908-2011-10), Chinese Ministry of Education via the Program for New Century Excellent Talents in University (Grant NCET-12-0079), and the Fundamental Research Funds for the Central Universities (DUT12LK51).

Literature Cited

1. Lee KI, Lee SW, Park MS, Chu CN. The development of air-breathing proton exchange membrane fuel cell (PEMFC) with a cylindrical configuration. *Int J Hydrogen Energy*. 2010;35:11844–11854.
2. Song C. Fuel processing for low-temperature and high-temperature fuel cells challenges, and opportunities for sustainable development in the 21st century. *Catal Today*. 2002;77:17–49.
3. Fu Q, Saltsburg H, Flytzani-Stephanopoulos M. Active nonmetallic Au and Pt species on ceria-based water-gas shift catalysts. *Science*. 2003;301:935–938.
4. Liu L, Hong L. Nickel phosphide catalyst for autothermal reforming of surrogate gasoline fuel. *AIChE J*. 2011;57:3143–3152.
5. Avgouropoulos G, Ioannides T, Papadopoulou C, Batista J, Hocevar S, Matralis HK. A comparative study of Pt/γ-Al_2O_3, Au/α-Fe_2O_3 and CuO-CeO_2 catalysts for the selective oxidation of carbon monoxide in excess hydrogen. *Catal Today*. 2002;75:157–167.
6. Watanabe M, Uchida H, Ohkubo K, Igarashi H. Hydrogen purification for fuel cells: selective oxidation of carbon monoxide on Pt-Fe/zeolite catalysts. *Appl Catal B: Environ*. 2003;46:595–600.
7. Ouyang X, Bednarova L, Besser RS, Ho P. Preferential Oxidation (PrOx) in a thin-film catalytic microreactor: advantages and limitations. *AIChE J*. 2005;51:1758–1772.
8. Park ED, Lee D, Lee HC. Recent progress in selective CO removal in a H2-rich stream. *Catal Today*. 2009;139:280–290.
9. Veselovskyi VL, Ischenko EV, Gayday SV, Lisnyak VV. A high efficient two phase CuO/$Cu_2(OH)_3NO3(Co_2+/Fe_3+)$ composite catalyst for CO-PROX reaction. *Catal Commun*. 2012;18:137–141.
10. Woods MP, Gawade P, Tan B, Ozkan US. Preferential oxidation of carbon monoxide on Co/CeO_2 nanoparticles. *Appl Catal B: Environ*. 2010;97:28–35.
11. Martínez-Arias A, Barrio L, Estrella M, Zhou G, Fonseca JJ, Hanson JC, Rodriguez JA. Inverse CeO_2/CuO catalyst as an alternative to classical direct configurations for preferential oxidation of CO in hydrogen-rich stream. *J Am Chem Soc*. 2010;132:34–35.
12. Benedetto ADi, Landi G, Lisi L, Russo G. Role of CO_2 on CO preferential oxidation over CuO/CeO_2 catalyst. *Appl Catal B: Environ*. 2013;142–143:169–177.
13. Ayastuy JL, Fernández-Puertas E, González-Marcos MP, Gutiérrez-Ortiz MA. Transition metal promoters in CuO/CeO_2 catalysts for CO removal from hydrogen streams. *Int J Hydrogen Energy*. 2012;37:7385–7397.
14. Si R, Raitano J, Yi N, Zhang L, Chan SW, Flytzani-Stephanopoulos M. Structure sensitivity of the low-temperature water-gas shift reaction on Cu-CeO_2 catalysts. *Catal Today*. 2012;180:68–80.
15. Zhang Q, Liu X, Fan W, Wang, Y. Manganese-promoted cobalt oxide as efficient and stable non-noble metal catalyst for preferential oxidation of CO in H_2 stream. *Appl Catal B: Environ*. 2011;102:207–214.
16. Guo Q, Liu Y. MnOx modified Co_3O_4-CeO_2 catalysts for the preferential oxidation of CO in H_2-rich gases. *Appl Catal B: Environ*. 2008;82:19–26.
17. Yao Z, Zhang X, Peng F, Yu H, Wang H, Yang J. Novel highly efficient alumina-supported cobalt nitride catalyst for preferential CO oxidation at high temperatures. *Int J Hydrogen Energy*. 2011;36:1955–1959.
18. Gómez LE, Tiscornia IS, Boix AV, Miró EE. Co/ZrO_2 catalysts coated on cordierite monoliths for CO preferential oxidation. *Appl Catal A: Gen*. 2011;401:124–133.
19. Zhou G, Xie H, Gui B, Zhang G, Zheng X. Influence of NiO on the performance of CoO-based catalysts for the selective oxidation of CO in H_2-rich gas. *Catal Commun*. 2012;19:42–45.
20. Gawade P, Bayram B, Alexander AMC, Ozkan US. Preferential oxidation of CO (PROX) over CoOx/CeO_2 in hydrogen-rich streams: effect of cobalt loading. *Appl Catal B: Environ*. 2012;128:21–30.
21. Mariño F, Descorme C, Duprez D. Supported base metal catalysts for the preferential oxidation of carbon monoxide in the presence of excess hydrogen (PROX). *Appl Catal B: Environ*. 2005;58:175–183.
22. Yen H, Seo Y, Kaliaguine S, Kleitz F. Tailored mesostructured copper/ceria catalysts with enhanced performance for preferential oxidation of CO at low temperature. *Angew Chem Int Ed*. 2012;51:12032–12035.
23. Gamarra D, Belver C, Fernández-García M, Martínez-Arias A. Selective CO oxidation in excess H_2 over copper-ceria catalysts: identification of active entities/species. *J Am Chem Soc*. 2007;129:12064–12065.
24. Yang F, Graciani J, Evans J, Liu P, Hrbek J, Sanz JF, Rodriguez JA. CO oxidation on inverse CeOx/Cu(111) catalysts: high catalytic activity and ceria-promoted dissociation of O_2. *J Am Chem Soc*. 2011;133:3444–3451.
25. Zhao ZK, Li Y, Bao T, Wang G, Muhammad T. Hierarchically nanoporous Co-Mn-O/FeOx as a high performance catalyst for CO preferential oxidation in H_2-rich stream. *Catal Commun*. 2014;46:28–31.
26. Zhao ZK, Bao T, Li Y, Min X, Zhao D, Muhammad T. The supported CeO_2/Co_3O_4-MnO_2/CeO_2 catalyst on activated carbon prepared by a successive-loading approach with superior catalytic activity and selectivity for CO preferential. *Catal Commun*. 2014;48:24–28.
27. Zhao ZK, Jin RH, Li Y, Dai YT, Muhammad T. Mesostructured Co-Ce-Zr-Mn-O composite as a potential catalyst for efficient removal of carbon monoxide from hydrogen-rich stream. *Catal Sci Technol*. 2013;3:2130–2139.
28. Zhao ZK, Lin XL, Zeng Y, Bao T, Dai YT, Jin RH, Muhammad T. Bismuth effect on the catalytic performance of the nanoparticulate Co-Mn/$Ce_{0.85}Zr_{0.15}O_2$ for CO preferential oxidation in simulated syngas. *Int J Hydrogen Energy*. 2013;38:1873–1882.
29. Zhao ZK, Bao T, Zeng Y, Wang GR, Muhammad T. Efficient cobalt-manganese oxide catalyst deposited on modified AC with unprecedented catalytic performance in CO preferential oxidation. *Catal Commun*. 2013;32:47–51.
30. Bao T, Zhao ZK., Dai YT, Lin XL, Jin RH, Wang GR, Muhammad T. Supported Co_3O_4-CeO_2 catalysts on modified activated carbon for CO preferential oxidation in H_2-rich gases. *Appl Catal B: Environ*. 2012;119–120:62–73.
31. Zhao ZK, Lin XL, Jin RH, Dai YT, Wang GR. Improvement of nano-particulate $Ce_xZr_{1-x}O_2$ composite oxides supported cobalt oxide catalysts for CO preferential oxidation in H_2-rich gases. *Catal Sci Technol*. 2012;2:554–563.
32. Zhao ZK, Jin RH, Bao T, Yang HL, Lin XL, Wang GR. Mesoporous $Ce_xMn_{1-x}O_2$ composites as novel alternative carriers of supported Co_3O_4 catalysts for CO preferential oxidation in H_2 stream. *Int J Hydrogen Energy* 2012;37:4774–4786.
33. Zhao ZK, Lin XL, Jin RH, Wang GR, Muhammad T. MO_x (M = Mn, Fe, Ni or Cr) improved supported Co_3O_4 catalysts on ceria-zirconia nanoparticulate for CO preferential oxidation in H_2-rich gases. *Appl Catal B: Environ*. 2012;115–116:53–62.
34. Zhao ZK, Jin RH, Bao T, Lin XL, Wang GR. Mesoporous ceria-zirconia supported cobalt oxide catalysts for CO preferential oxidation reaction in excess H_2. *Appl Catal B: Environ*. 2011;110:154–163.
35. Zhao ZK, Lin XL, Jin RH, Dai YT, Wang GR. High catalytic activity in CO PROX reaction of low cobalt-oxide loading catalysts supported on nano-particulate CeO_2–ZrO_2 oxides. *Catal Commun*. 2011;12:1448–1451.
36. Mao JP, Deng MM, Chen L, Liu Y, Lu Y. Novel Microfibrous-Structured Silver Catalyst for High Efficiency Gas-Phase Oxidation of Alcohols. *AIChE J*. 2010;56:1545–1556.
37. Tonetto GM, Ferreira ML, Atias JA, de Lasa HI. Effect of Steaming Treatment in the Structure and Reactivity of FCC Catalysts. *AIChE J*. 2006;52:754–768.
38. Feldheim DL. The new face of catalysis. *Science*. 2007;316:699–700.
39. Xie XW, Li Y, Liu ZQ, Haruta M, Shen WJ. Low-temperature oxidation of CO catalysed by Co_3O_4 nanorods. *Nature*. 2009;458:746–749.

40. Jafar HS, Rashidi M, Bahrami M. Platinum nanostructures at the liquid–liquid interface: catalytic reductionof *p*-nitrophenol to p-aminophenol. *J Mater Chem*. 2011;21:16170–16176.
41. Fallah B, Falamaki C. A new nano-($2Li_2O$/MgO) catalyst/porous alpha-alumina composite for the oxidative coupling of methane reaction. *AIChE J*. 2012;58:1248–1261.
42. Zhang WX, Chen GD, Yang ZH, Zeng CY. A novel approach to well-aligned TiO_2 nanotube arrays and their enhanced photocatalytic performances. *AIChE J*. 2013;59:2134–2144.
43. Ta N, Zhang ML, Li J, Li HJ, Li Y, Shen WJ. Morphology-dependent redox and catalytic properties of CeO2 nanostructures: nanowires, nanorods and nanoparticles. *Catal Today*. 2009;148:179–183.
44. Lv YG, Li Y, Ta N, Shen WJ. Co_3O_4 nanosheets: synthesis and catalytic application for CO oxidation at room temperature. *Sci China Chem*. 2014;57:873–880.
45. He ZQ, Wen LN, Wang D, Xue YJ, Lu QW, Wu CW, Chen JM, Song S. Photocatalytic reduction of CO_2 in aqueous solution on surface-fluorinated anatase TiO_2 nanosheets with exposed {001} facets. *Energy Fuels*. 2014;28:3982–3993.
46. Yu YL, Zhang P, Guo LM, Chen ZD, Wu Q, Ding YH, Zheng WJ, Cao YA. The design of TiO_2 nanostructures (nanoparticle, nanotube, and nanosheet) and their photocatalytic activity. *J Phys Chem C*. 2014;118:12727–12733.
47. Zhang H, Jin MS, Liu HY, Wang JG, Kim MJ, Yang DR, Xie ZX, Liu JY, Xia YN. Facile synthesis of Pd-Pt alloy nanocages and their enhanced performance for preferential oxidation of CO in excess hydrogen. *ACS Nano*. 2011;5:8212–8222.
48. Xu PP, Ye K, Cao DX, Huang JC, Liu T, Cheng K, Yin J, Wang GL. Facile synthesis of cobalt manganese oxides nanowires on nickel foam with superior electrochemical performance. *J Power Sources*. 2014;268:204–211.
49. Li GN, Li L, Shi JJ, Yuan YY, Li YS, Zhao WR, Shi JL. One-pot pyrolytic synthesis of mesoporous MCo_2O_4 (M = Mn, Ni, Fe, Cu) spinels and its high efficient catalytic properties for CO oxidation at low temperature. *J Mol Catal A: Chem*. 2014;390:97–104.
50. Tian ZY, Ngamou PHT, Vannier V, Kohse-Hönghaus K, Bahlawane N. Catalytic oxidation of VOCs over mixed Co-Mn oxides. *Appl Catal B: Environ*. 2012;117–118:125–134.
51. Morales F, Grandjean D, Mens A, Groot de FMF, Weckhuysen BM. X-ray absorption spectroscopy of Mn/Co/TiO_2 Fischer-Tropsch catalysts: relationships between preparation method, molecular structure, and catalyst performance. *J Phys Chem B*. 2006;110:8626–8639.
52. Morales F, Smit de E, Groot de MF, Visser T, Weckhuysen BM. Effects of manganese oxide promoter on the CO and H_2 adsorption properties of titania-supported cobalt Fischer-Tropsch catalysts. *J Catal*. 2007;246:91–99.
53. Todorova S, Kolev H, Holgado JP, Kadinov G, Bonev C, Pereñíguez R, Caballero A. Complete n-hexane oxidation over supported Mn-Co catalysts. *Appl Catal B: Environ*. 2010;94:46–54.
54. Gómez LE, Miró EE, Boix AV. Spectroscopic characterization of Mn-Co-Ce mixed oxides, active catalysts for COPROX reaction. *Int J Hydrogen Energy*. 2013;38:5645–5654.
55. Guo Q, Chen SQ, Liu Y, Wang YQ. Stability of Co-Ce-Mn mixed-oxide catalysts for CO preferential oxidation in H_2-rich gases. *Chem Eng J*. 2010;165:846–850.
56. Park JW, Jeong JH, Yoon WL, Rhee YW. Selective oxidation of carbon monoxide in hydrogen-rich stream over Cu-Ce/γ-Al_2O_3 catalysts promoted with cobalt in a fuel processor for proton exchange membrane fuel cells. *J Power Sources*. 2004;132:18–28.
57. Avgouropoulos G, Ioannides T, Papadopoulou C, Batista J, Hocevar S, Matralis HK. A comparative study of Pt/γ-Al_2O_3, Au/α-Fe_2O_3 and CuO-CeO_2 catalysts for the selective oxidation of carbon monoxide in excess hydrogen. *Catal Today*. 2002;75:157–167.
58. Jung CR, Han J, Nam SW, Lim TH, Hong SA, Lee HI. Selective oxidation of CO over CuO-CeO_2 catalyst: effect of calcination temperature. *Catal Today*. 2004;93–95:183–190.
59. Snytnikov PV, Popova MM, Men Y, Rebrov EV, Kolb G, Hessel V, Schouten JC, Sobyanin VA. Preferential CO oxidation over a copper-cerium oxide catalyst in a microchannel reactor. *Appl Catal A: Gen*. 2008;350:53–62.
60. Jansson J, Palmqvist AEC, Fridell E, Skoglundh M, Österlund L, Thormählen P, Langer V. On the catalytic activity of Co_3O_4 in low-temperature CO oxidation. *J Catal*. 2002;211:387–397.

Manuscript received Aug. 14, 2014, and revision received Sep. 24, 2014.